

Langmuir wave filamentation in the kinetic regime. I. Filamentation instability of Bernstein-Greene-Kruskal modes in multidimensional Vlasov simulations

Denis A. Silantyev,¹ Pavel M. Lushnikov,^{1,*} and Harvey A. Rose^{2,3}

¹*Department on Mathematics and Statistics, University of New Mexico, New Mexico 87131, USA*

²*Theoretical Division, Los Alamos National Laboratory, MS-B213, Los Alamos, New Mexico, 87545*

³*New Mexico Consortium, Los Alamos, New Mexico 87544, USA*

(Dated: February 1, 2022)

A nonlinear Langmuir wave in the kinetic regime $k\lambda_D \gtrsim 0.2$ may have a filamentation instability, where k is the wavenumber and λ_D is the Debye length. The nonlinear stage of that instability develops into the filamentation of Langmuir waves which in turn leads to the saturation of the stimulated Raman scattering in laser-plasma interaction experiments. Here we study the linear stage of the filamentation instability of the particular family [1] of Bernstein-Greene-Kruskal (BGK) modes [2] that is a bifurcation of the linear Langmuir wave. Performing direct 2+2D Vlasov-Poisson simulations of collisionless plasma we find the growth rates of oblique modes of the electric field as a function of BGK's amplitude, wavenumber and the angle of the oblique mode's wavevector relative to the BGK's wavevector. Simulation results are compared to theoretical predictions.

I. INTRODUCTION

Consider a Langmuir wave [3, 4] (LW) wave packet with a typical wavenumber k . If $k\lambda_D \lesssim 0.2$, then the hydrodynamic approximation (the “fluid” regime) to LW dynamics is valid, where λ_D is the Debye length. In that regime a LW has a nonlinear frequency shift $\Delta\omega_{fluid}$, due to electron dynamics, proportional to the squared LW electric field amplitude E , i.e. $\Delta\omega_{fluid} \propto |E|^2$ [5–7]. As shown in Ref. [8], the transition from the fluid to the “kinetic” regime occurs at $k\lambda_D \sim 0.2$ when trapped electron effects cannot be ignored. The LW frequency shift due to electron trapping, $\Delta\omega_{trapped}$, perturbatively varies as $\Delta\omega_{trapped} \propto |E|^{1/2}$ [1, 6, 8–10] with possible higher order corrections as discussed in Ref. [11]. Thus $\Delta\omega_{trapped}$ at $k\lambda_D \gtrsim 0.2$ may dominate [8, 11–14] over $\Delta\omega_{fluid}$. Negative $\Delta\omega_{trapped}$, with positive diffraction, imply LW filamentation [8, 15–17]. 3D particle-in-cell (PIC) [18] simulation results have been interpreted as showing that the trapped electron LW filamentation instability can saturate [19, 20] stimulated Raman backscatter (SRS) [21] by reducing the LWs coherence. In actual plasma, the SRS daughter LW is subject to other instabilities as well, such as LW-ion-acoustic decay (LDI). Fluid and kinetic regime LDI have been observed in SRS simulations [19, 22] while kinetic regime LDI has been experimentally [23] noted [12].

Additional complexity in the interpretation of experimental data gathered from laser-plasma interaction arises from instabilities of the laser beam [24, 25] coupled [26–28] to relatively low frequency ion-acoustic waves. Since direct experimental data pointing to kinetic LW filamentation has not been available, first principles simulation of pure LW dynamics is perhaps the cleanest way to “see” this phenomenon. Fully nonlinear PIC simulations [16] with Bernstein-Greene-Kruskal (BGK) mode [2] initial

conditions have shown qualitative agreement with LW filamentation theory [8, 15], but the theory's finer points, such as instability thresholds, require a noise free model, namely the Vlasov simulations.

Here we address LW filamentation in the kinetic regime with $k\lambda_D > 0.3$ by studying the filamentation instability of BGK modes using 2+2D (two velocity and two spatial dimensions) spectral Vlasov simulations. Our simulations only include collisionless electrostatic electron dynamics in a static neutralizing ion background, thereby excluding the LW ion-acoustic decay and ponderomotive LW filamentation instabilities, amongst others. BGK modes are constructed following the approach of Ref. [1] to approximate the adiabatically slow pumping by SRS. We concentrate on the linear stage of the filamentation instability development while observing strong LW filamentation in the nonlinear stage. Also in the second paper (Part II) of the series, we consider dynamically prepared BGK-like initial conditions created with slow SRS-like pumping (similar to Ref. [17]) and study the filamentation instability of those waves comparing both with the results of this paper for BGK modes and the results of Ref. [17].

The paper is organized as follows. Section II introduces the Vlasov-Poisson system and its general BGK solutions (equilibria). In Section III A we recall a special family [1] of 1+1D BGK modes that bifurcate from linear LW. We describe the analytical and numerical construction of these modes. Section III B outlines their nonlinear dispersion relation and Section III C provides filamentation's definition and analytical results on its growth rate. In Section IV we provide results of 2 + 2D Vlasov simulations. Section IV A is devoted to the Vlasov simulations settings and our numerical method. Section IV B addresses filamentation instability results and their comparison with theory. Section IV C provides a comparison of the growth rates obtained in Section IV B with the growth rates from PIC code simulations of Ref. [16]. In Section V the main results of the paper are discussed.

* plushnik@math.unm.edu

II. BASIC EQUATIONS

The Vlasov equation for the phase space distribution function $f(\mathbf{r}, \mathbf{v}, t)$, in units such that electron mass m_e and charge e are normalized to unity, the spatial coordinate $\mathbf{r} = (x, y, z)$ to the electron Debye length λ_D , the time t to reciprocal electron plasma frequency, $1/\omega_{pe}$, [29] and the velocity $\mathbf{v} = (v_x, v_y, v_z)$ is normalized to the electron thermal speed v_e , is

$$\left\{ \frac{\partial}{\partial t} + \mathbf{v} \cdot \nabla + \mathbf{E} \cdot \frac{\partial}{\partial \mathbf{v}} \right\} f = 0, \quad (1)$$

where \mathbf{E} is the electric field scaled to $k_B T_e / (\lambda_D e)$. Here T_e is the background electron temperature and k_B is the Boltzmann constant. Magnetic field effects are ignored for clarity. Then, in the electrostatic regime,

$$\mathbf{E} = -\nabla \Phi, \quad (2)$$

with the electrostatic potential Φ given by Poisson's equation

$$\nabla^2 \Phi = 1 - \rho, \quad (3)$$

and electron density, ρ , is given by

$$\rho(\mathbf{r}, t) = \int f(\mathbf{r}, \mathbf{v}, t) d\mathbf{v}. \quad (4)$$

The usual factor of 4π is absent from equation (3) because of the chosen normalization and 1 in equation (3) comes from the neutralizing ion background.

Equations (1)-(4) form the closed Vlasov-Poisson system. Its finite amplitude travelling wave solutions, moving with phase velocity, v_φ , are called Bernstein-Greene-Kruskal (BGK) modes [2]. Here we assume without loss of generality that z is chosen in the direction of v_φ so that f assumes the form $f(\mathbf{r}_\perp, z - v_\varphi t, \mathbf{v})$, with $\mathbf{r}_\perp \equiv (x, y)$, and equation (1) reduces to

$$(v_z - v_\varphi) \frac{\partial}{\partial z} f + \mathbf{v}_\perp \cdot \nabla f + \mathbf{E} \cdot \frac{\partial}{\partial \mathbf{v}} f = 0. \quad (5)$$

The general solution of equations (2) and (5) is given by $f = g(W)$, where g is an arbitrary function of the single scalar argument

$$W \equiv \frac{(v_z - v_\varphi)^2}{2} + \frac{\mathbf{v}_\perp^2}{2} + \Phi(\mathbf{r}_\perp, z - v_\varphi t) \quad (6)$$

which is the single particle energy (kinetic energy in the moving reference frame plus electrostatic energy).

BGK modes are obtained if we require $g(W)$ to satisfy equations (3) and (4) [2]. That requirement still allows a wide variety of solutions.

III. BGK MODE LINEAR FILAMENTATION INSTABILITY

Our goal is to study the transverse stability of BGK modes. In general, a linear instability is specific to a given

BGK mode. We choose a BGK mode that is dynamically selected (at least approximately) by SRS with z being the direction of laser beam propagation in plasma. The simplest BGK family has a nontrivial solution f_{BGK} in $1 + 1D$ (one space and one velocity dimension [2]) with no dependence on the transverse coordinate \mathbf{r}_\perp , while the dependence on the transverse velocity \mathbf{v}_\perp being trivially Maxwellian as follows

$$f = f_{BGK}(z - v_\varphi t, v_z) \frac{\exp(-\mathbf{v}_\perp^2/2)}{2\pi}. \quad (7)$$

Our initial model [1] of the SRS daughter LW in a laser speckle is presented in Eq. (12) below. If a time-dependent Vlasov equation solution has a symmetry, e.g., in $2 + 2D$ (two space and two velocity dimensions) when the initial condition (and possible external potential) only depend on one spatial coordinate z , or in $3 + 3D$ a cylindrically symmetric configuration, then an instability may break that symmetry, allowing for a determination of growth rate. The former, revisited here, was explored in $2 + 2D$ Vlasov simulations [17], while the latter was observed [19] in $3D$ PIC, SRS single speckle simulations. In addition, we present LW filamentation growth rates of linear fluctuations about a particular class of BGK modes, recalled in the next Section III A.

A. Construction of 1+1D BGK

The beating of laser and SRS light provides a source of LWs thus pumping BGK modes. Following Ref. [1], we assume that the laser intensity is just above SRS instability threshold. Then the pumping of LWs is slow and can be idealized as a travelling wave sinusoidal external potential Φ_{ext} , with amplitude ϕ_{pump} , phase speed v_φ and wavenumber k_z such that

$$\Phi_{ext} = \phi_{pump} \cos[k_z(z - v_\varphi t)], \quad k_z = |\mathbf{k}|. \quad (8)$$

The total electrostatic potential, Φ , is given by

$$\Phi = \Phi_{ext} + \Phi_{int}, \quad (9)$$

where the internal potential Φ_{int} is determined from Poisson's equation (10), where $f_{1D}(z, v_z, t)$ is the $1D$ electron phase space distribution function.

$$\frac{\partial^2 \Phi_{int}}{\partial z^2} = 1 - \int f_{1D} dv_z, \quad (10)$$

Inertial confinement fusion applications require a dynamic laser beam smoothing [30–32] resulting in a time-dependent speckle field of laser intensity. Φ_{ext} attains a local maximum in a laser speckle, which is a local maximum of laser beam intensity. Intense speckles have a width approximately $F\lambda_0$, with F the optic f -number (the ratio of the focal length of the lens divided by the lens diameter) and λ_0 the laser wavelength. The temporal scale t_c of beam smoothing is typically large compared

with the inverse growth rate $1/\gamma_{SRS}$ of SRS (e.g. for the National Ignition Facility [31, 32] $t_c \sim 4\text{ps}$ and typically $1/\gamma_{SRS} \sim 0.03\text{ps}$). It implies that the speckle can be considered as time-independent which we assume below. Electrons, with the typical speed v_e , cross a speckle width in a dimensional time scale $1/\nu_{SideLoss} \propto F\lambda_0/v_e$. As a result, f_{1D} tends to relax to the background distribution function, f_0 , assumed Maxwellian,

$$f_0(v_z) = \frac{\exp(-v_z^2/2)}{\sqrt{2\pi}} \quad (11)$$

at the rate $\nu_{SideLoss}$. These considerations motivate our 1 + 1D model of BGK generation by introducing the relaxation term $-\nu_{SideLoss}[f_{1D}(z, v_z, t) - f_0(v_z)]$ into the Vlasov equation (1) as follows. In the wave frame (switching to that frame implies $z \rightarrow z + v_\varphi t$ and $v_z \rightarrow v_z + v_\varphi$),

$$\left\{ \frac{\partial}{\partial t} + v_z \frac{\partial}{\partial z} - \frac{\partial \Phi}{\partial z} \frac{\partial}{\partial v_z} \right\} f_{1D}(z, v_z, t) = -\nu_{SideLoss}[f_{1D}(z, v_z, t) - f_0(v_z + v_\varphi)]. \quad (12)$$

Let f_{eq} be a time independent solution of Eq. (12). In the double limit

$$f_{BGK} = \lim_{\phi_{pump} \rightarrow 0} \lim_{\nu_{SideLoss} \rightarrow 0} f_{eq}, \quad (13)$$

a particular BGK mode which bifurcates [33, 34] from a linear LW, f_{BGK} , may be obtained [1]. This mode correspond to the adiabatically slow pumping by SRS. It depends on (z, v_z) only through the single particle energy, W ,

$$W = \Phi(z) + v_z^2/2 \quad (14)$$

which is the restriction of equation (6) to 1+1D case in the wave frame with $\Phi(\mathbf{r}_\perp, z - v_\varphi t) \rightarrow \Phi(z)$.

There are two methods to construct BGK modes in question. First method is numerical one and implies that we numerically solve equations (8)-(12) for each values of ϕ_{pump} and $\nu_{SideLoss}$ followed by taking numerically the double limit (13). Second method is analytical one and is based on the integration along the particle orbits of the time independent solution of Eq. (12), where the double limit (13) is evaluated analytically. We investigated both methods, found that they give similar results, but choose below to focus on the second method only since it is a simpler to implement and free of numerical issues.

The electrostatic potential Φ traps electrons with velocities close enough to v_φ such that they cannot go over barriers created by Φ . Thus for different electrons there are both passing orbits outside the trapping region and periodic orbits inside the trapping region. Recall that passing orbits can have either positive or negative velocities, and this must be specified along with W . It was shown in Refs. [35] and [1] that taking the double limit (13) in the equation Eq. (12) we get

$$f_{BGK}(W) = \oint_W f_0[v(s) + v_\varphi] ds / T(W). \quad (15)$$

The integral sign here denotes integration around a particular orbit with constant W . The time-like characteristic variable s , used in integration, parametrizes a particular orbital location $(z(s), v(s))$ through the characteristic equations

$$dz/ds = v, \quad dv/ds = -d\Phi/dz. \quad (16)$$

Also $T(W)$ denotes the orbit's period,

$$T(W) = \oint_W ds. \quad (17)$$

Here and throughout the remaining part of Section III we replace v_z by $v(\cdot)$ when it describes the velocity of a particular electron with energy W as a function of some parameter (s or z), while we think of v_z as independent variable in the rest of the formulas. Also we abuse notation and use the same symbols for v and f_{BGK} irrespective of their parametrization by different variables. Φ is assumed periodic so that all orbits are closed by periodicity (including the passing orbits).

Assume $\Phi(z)$ is the given function of z . Then using Eq. (14), changing the integration variable from s to z in Eqs. (15) and (17), we can express $T(W)$ and $f_{BGK}(z, v_z) \equiv f_{BGK}(W)$ at any point (z, v_z) in the phase space as follows (see Fig. 1)

$$T(W) = \begin{cases} 4 \int_0^{z_{max}} \frac{dz}{v(z)}, & \Phi_{min} < W < \Phi_{max}, \\ \int_0^{L_z} \frac{dz}{v(z)}, & W > \Phi_{max}, \end{cases} \quad (18)$$

$$f_{BGK}(W)T(W) = \begin{cases} 2 \int_0^{z_{max}} \frac{f_0[v_\varphi + v(z)] + f_0[v_\varphi - v(z)] dz}{v(z)}, & \Phi_{min} < W < \Phi_{max}, \\ \int_0^{L_z} \frac{f_0[v_\varphi + v(z)] dz}{v(z)}, & W > \Phi_{max} \text{ and } v_z > v_\varphi, \\ \int_0^{L_z} \frac{f_0[v_\varphi - v(z)] dz}{v(z)}, & W > \Phi_{max} \text{ and } v_z < v_\varphi, \end{cases} \quad (19)$$

and $v(z)$ is determined from Eq. (14) as

$$v(z) = \sqrt{2[W - \Phi(z)]}, \quad (20)$$

with $\Phi_{min} \equiv \min_z \Phi(z)$, $\Phi_{max} \equiv \max_z \Phi(z)$, $L_z \equiv \frac{2\pi}{k_z}$. We assume that $\Phi(z)$ has a single local maximum and a single local minimum per period L_z . Also z_{max} is obtained by numerically inverting $\Phi(z_{max}) = W$ (see Fig. 1 for the illustration). Note that it is also possible to integrate Eqs. (15) and (17) directly in s variable which has more compact form compared to Eqs. (18)-(19). However, we chose to use Eqs. (18)-(20) because it is easier to implement a high-order numerical scheme for integrals (18) and (19) that depend only on one independent variable rather than calculating integrals in Eqs. (15)-(17) that require two-step process, first numerically finding orbits $(z(s), v(s))$ and then computing the integrals.

The amplitudes of Fourier harmonics of $\Phi(z)$ are rapidly decaying [1], so we start by constructing a BGK

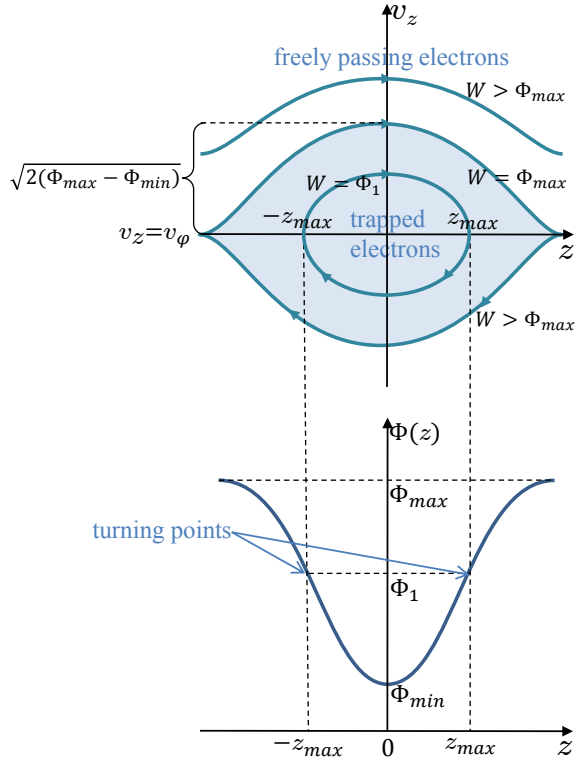


FIG. 1. (Color online) Schematics of the electric potential and the corresponding trapping region of $f_{BGK}(z, v_z)$.

mode approximately by taking into account only the first harmonic

$$\Phi(z) = -\phi_0 \cos(k_z z) \quad (21)$$

parametrized by the amplitude ϕ_0 . Then the comparison with definitions in Eq. (20) implies that $\Phi_{min} = -\phi_0$, $\Phi_{max} = \phi_0$, $v(z) = \sqrt{2(W + \phi_0 \cos(k_z z))}$ and $z_{max} = \frac{1}{k_z} \arccos(\frac{-W}{\phi_0})$.

Integrating f_{BGK} over v_z that was obtained from Eqs. (18)-(20) and using the Poisson's equation (10), we get the corresponding electrostatic potential $\Phi_{approx}(z)$ of the approximate BGK solution. One can use k_z as the free parameter to rescale the solution in such a way that the amplitude of the first harmonic in the electrostatic potential is equal to ϕ_0 as was assumed in Eq. (21).

The result is however only approximate because of higher order Fourier harmonics beyond the fundamental one assumed for $\Phi(z)$ in Eq. (21). Our calculations show that the second harmonic in $\Phi(z)$ is typically 2-3 orders of magnitude less compared to the first one even for ϕ_0 of order 1, which validates our initial assumption. We found it satisfactory for the purpose of the subsequent results of this paper to stop the process of BGK construction at this point. However we also used $\Phi_{approx}(z)$ to obtain the corresponding updated $f_{BGK}(z, v_z)$ from Eqs. (18)-(20), calculated second iteration of $\Phi_{approx}(z)$, and so on. We found that typically ~ 20 iterations is sufficient to converge $\Phi_{approx}(z)$ within 10^{-15} relative pointwise

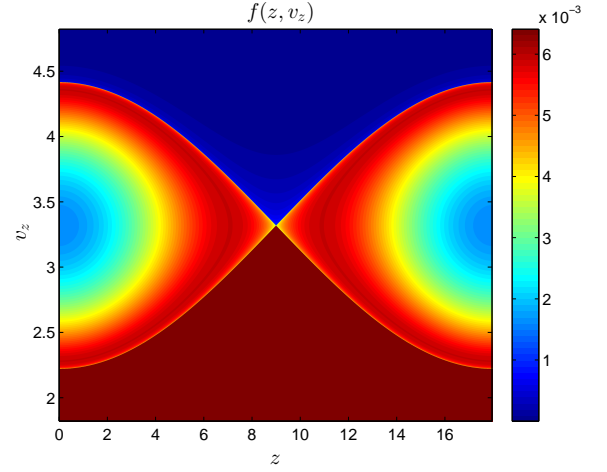


FIG. 2. (Color online) The phase space density distribution $f_{BGK}(z, v_z)$ of BGK mode with $k_z = 0.35$, $\phi_0 = 0.3$, $v_\phi = 3.321836 \dots$

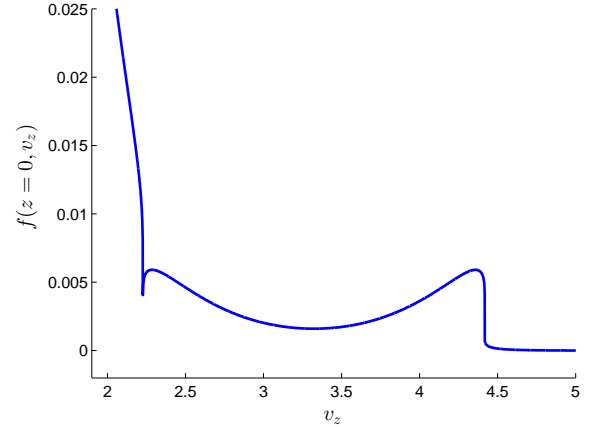


FIG. 3. Cross-section of $f_{BGK}(z = 0, v_z)$ for BGK mode with $k_z = 0.35$, $\phi_0 = 0.3$, $v_\phi = 3.321836 \dots$

error over z (with the relative error being $\sim 1\%$ after first iteration) to the exact BGK mode. In this way one can construct a BGK mode for given values of ϕ_0 and v_ϕ as the input parameters producing the value k_z as the output parameter together with f_{BGK} . If one needs to find f_{BGK} with the specified value of $k_z = k_{z,input}$ then Newton iterations are performed to find a root of $k_{z,input} - k_{z,output}(\phi_0, v_\phi) = 0$ as a function of either ϕ_0 or v_ϕ keeping the other variable fixed. Here $k_{z,output}(\phi_0, v_\phi)$ is the value of k_z obtained for given ϕ_0 and v_ϕ from the procedure described above.

An example of BGK mode constructed using this approach with Newton iterations over v_ϕ for $k_{z,input} = k_z = 0.35$, $\phi_0 = 0.3$ and resulting $v_\phi = 3.321836 \dots$ is shown in Figs. 2-3. Fig. 2 shows $f_{BGK}(z, v_z)$ around the trapping region with a separatrix $\Phi(z) + v_z^2/2 = W = \Phi_{max}$. Fig. 3 shows the widest cross-section of the trapping region at $z = 0$.

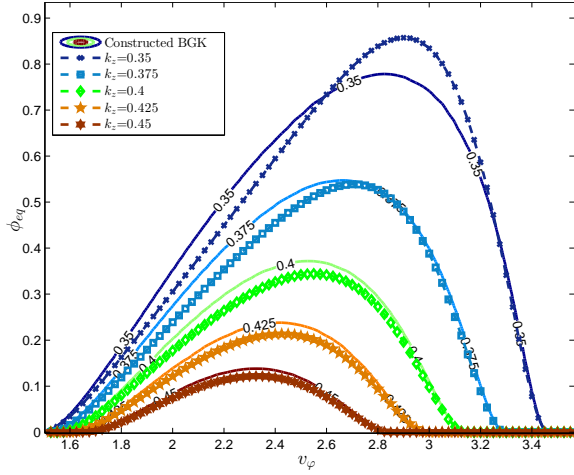


FIG. 4. (Color online) LW and EAW potential amplitude versus phase velocity for various k_z . Solid lines represent constructed BGK family dispersion relation, dashed - approximation of dispersion relation by formula (22).

B. BGK dispersion relation and nonlinear frequency shift

The dispersion relation of the particular family of BGK modes in question has been presented in Refs. [1] and [8]. Unlike the linear regime, in which the parameters k_z and v_{ϕ} are related via well-known ϕ_{eq} -independent dispersion relations [36, 37], a BGK mode's dispersion relation is amplitude dependent. The BGK mode identified by Eqs. (12) and (13) is undamped and has a nonlinear dispersion relation determined [33, 34] by setting the real part of the dielectric function, ε , to zero. Recall that we define the nonlinear dielectric function ε as $\Phi = \Phi_{ext}/\varepsilon$ with Φ_{ext} being the external pump from SRS, Eq. (8). To lowest order in $\sqrt{\phi_{eq}}$ using f_{BGK} given by Eqs. (18)-(21) one obtains [1] that,

$$0 = \text{Re}[\varepsilon] \approx \text{Re}[\varepsilon_0] + 1.76 f_0''(v_{\phi}) \sqrt{\phi_{eq}}/k_z^2, \quad (22)$$

where

$$\varepsilon_0(k_z, \omega) = 1 - \Xi_0(v_{\phi})/k_z^2, \quad (23)$$

$$\Xi_0(v) = Z'(v/\sqrt{2})/2,$$

$$Z(v) = e^{-v^2} \sqrt{\pi} (i - \text{erfi}(v)) = e^{-v^2} (i\sqrt{\pi} - 2 \int_0^v e^{t^2} dt).$$

Z is the plasma dispersion function [38] and ε_0 is the linear dielectric function.

Eq. (22) can be solved for $\phi_{eq}(k_z, v_{\phi})$. These solutions are illustrated in Fig. 4 by dashed lines with markers for various values of k_z together with solid lines corresponding to the BGK modes that were constructed numerically following the procedure in III A with the same values of k_z and v_{ϕ} . For $k_z = 0.35$ the maximum amplitude of the constructed BGK is $\phi_{eq} \approx 0.78$ at $v_{\phi} \approx 2.85$ while Eq.

(22) overestimates the maximum ϕ_{eq} at 0.85. The correspondence of solutions of Eq. (22) and values of v_{ϕ} for the constructed BGKs for small ϕ_{eq} is quite good. For each k_z and ϕ_{eq} less than the maximum amplitude, we have two solutions for v_{ϕ} , the larger value corresponding to the nonlinear LW wave and the smaller one corresponding to the electron acoustic [39] wave (EAW), similar to two solutions of the Vlasov dispersion relation $\text{Re}[\varepsilon_0(k_z, \omega)] = 0$ for a given k_z (see Fig. 2 in Ref. [40]).

Alternatively, v_{ϕ} may be considered as a function of k_z and ϕ_{eq} , i.e. $v_{\phi}(k_z, \phi_{eq})$, by inverting the graph shown in Fig. 4. Since a travelling wave's angular frequency, ω , is always the product of wavenumber and phase velocity, $\omega = k_z v_{\phi}$, one may re-express the nonlinear dispersion relation as a wavenumber and amplitude dependent ω ,

$$\omega(k_z, \phi_{eq}) = k_z v_{\phi}(k_z, \phi_{eq}). \quad (24)$$

We define the nonlinear frequency shift as

$$\Delta\omega^{BGK} = \omega(k_z, \phi_{eq}) - \omega_0, \quad (25)$$

where $\omega_0 = \omega(k_z, \phi_{eq} = 0)$. For $k_z = 0.35$, $\omega_0 = 1.21167$.

Expanding $\text{Re}[\varepsilon_0(k_z, \omega)]$ in Eq. (22) in a Taylor series at $\omega = \omega_0$, taking into account that $\text{Re}[\varepsilon_0(k_z, \omega_0)] = 0$, we get an approximation of $\Delta\omega^{BGK}$ given by

$$\Delta\omega_{NL}^{Rose} = -1.76 \left[\frac{\partial \text{Re}[\varepsilon_0(\omega_0)]}{\partial \omega} \right]^{-1} f_0''(v_{\phi}) \frac{\sqrt{\phi_{eq}}}{k_z^2}, \quad (26)$$

as presented in Eq. (50) of Ref. [1] and Eq. (9) and Fig. 5 of Ref. [8]. For $k_z = 0.35$, $\frac{\partial \text{Re}[\varepsilon_0(\omega_0)]}{\partial \omega} = 2.335$.

In earlier works of Morales and O'Neil [10] and Dewar [6] an approximation for the nonlinear frequency shift of large-amplitude EPW was derived

$$\Delta\omega_{NL}^{Dewar} = -\alpha \left[\frac{\partial \text{Re}[\varepsilon_0(\omega_0)]}{\partial \omega} \right]^{-1} f_0''(v_{\phi}) \frac{\sqrt{\phi_{eq}}}{k_z^2}, \quad (27)$$

where $\alpha = 0.77\sqrt{2} = 1.089$ and $\alpha = 1.163\sqrt{2} = 1.645$ for the “adiabatic” and “sudden” excitation of nonlinear LW, respectively. The derivation was also summarized in Ref. [41] and used in Ref. [17]. In Ref. [1] after Eq. (48) H. Rose discusses the source of the discrepancy between 1.76 coefficient in Eq. (26) and 1.645 in Eq. (27).

C. Trapped electron filamentation instability

LW filamentation instability theory has been presented in Refs. [8] and [17], but we believe that a more cogent and general result was obtained in Ref. [15], which we now review.

Let x denote a direction perpendicular to the LW propagation direction, the z axis, with wave amplitude ϕ_{eq} , the maximum value of $\Phi(z)$ over z (in particular case given by Eq. (21), $\phi_{eq} = \phi_0$). Near the equilibrium (BGK mode) in the moving frame, let

$$\Phi = \text{Re} \{ \exp(i\mathbf{k} \cdot \mathbf{r}) [\phi_{eq} + \delta\phi(t) \exp(i\delta\mathbf{k} \cdot \mathbf{r})] \}, \quad (28)$$

where \mathbf{k} is parallel to z direction and $\delta\mathbf{k}$ is responsible for the transverse perturbations with the amplitude $\delta\phi(t)$. Let $\delta\phi \sim \exp(\gamma t)$. In Ref. [15] it was shown that

$$(\gamma + \nu_{\text{residual}})^2 = -D \left(\phi_{eq} \frac{\partial \omega}{\partial \phi_{eq}} + D \right), \quad (29)$$

wherein the generalized diffraction operator, D ,

$$2D = \omega(|\mathbf{k} + \delta\mathbf{k}|, \phi_{eq}) + \omega(|\mathbf{k} - \delta\mathbf{k}|, \phi_{eq}) - 2\omega(|\mathbf{k}|, \phi_{eq}) \quad (30)$$

reduces to the diffraction coefficient, $(|\delta\mathbf{k}_\perp|^2/2|\mathbf{k}|)(\partial\omega/\partial|\mathbf{k}|) + (\delta k_z^2/2)\partial^2\omega/\partial|\mathbf{k}|^2$, for small $|\delta\mathbf{k}|$. When $\delta\mathbf{k} \cdot \mathbf{k} = 0$, Eq. (30) simplifies to

$$D = \omega(|\mathbf{k} + \delta\mathbf{k}|, \phi_{eq}) - \omega(|\mathbf{k}|, \phi_{eq}), \quad (31)$$

and the (possible) instability is customarily called filamentation, our main regime of interest.

Also assuming $\phi_{eq} \ll 1$ in addition to $\delta\mathbf{k} \cdot \mathbf{k} = 0$ and $|\delta\mathbf{k}| \ll 1$, we can approximate Eq. (31) as follows

$$\begin{aligned} D &\approx D_{lin} = \frac{1}{2k_z} \frac{\partial \omega(|\mathbf{k}|, 0)}{\partial |\mathbf{k}|} \Big|_{|\mathbf{k}|=k_z} |\delta\mathbf{k}|^2 \\ &= \frac{v_g}{2k_z} |\delta\mathbf{k}|^2, \quad v_g \equiv \partial \omega(|\mathbf{k}|, 0) / \partial |\mathbf{k}|, \end{aligned} \quad (32)$$

where v_g is the group velocity corresponding to the dispersion relation (22) at $\phi_{eq} = 0$, $v_g = 1.008$ for $k_z = 0.35$.

The residual damping, ν_{residual} , from Eq. (29) is model dependent. For example, if the double limit of Eq. (13) stops short of zero value, but with

$$\frac{\nu_{\text{residual}}}{\omega_{\text{bounce}}} \ll 1, \quad \frac{\phi_{\text{pump}}}{\phi_{eq}} \ll 1, \quad \frac{\omega_{\text{bounce}}}{\omega_{pe}} = k_z \sqrt{\phi_{eq}}, \quad (33)$$

or in dimensional units, $\frac{\omega_{\text{bounce}}}{\omega_{pe}} = k_z \lambda_D \sqrt{e\phi_{eq}/k_B T_e}$. Then it follows from Eqs. (28), (71) of Ref. [1] and Fig. 3 of Ref. [1] that, for $v_\varphi \gtrsim 2.2$, in dimensional units,

$$\nu_{\text{residual}} \approx \frac{\omega_{pe}}{2} \text{Im}[\varepsilon] \gtrsim \frac{\nu_{\text{SideLoss}}}{\omega_{\text{bounce}}} \nu_{\text{Landau}}. \quad (34)$$

In Eq. (34), the Landau damping rate, ν_{Landau} , is evaluated for a linear LW with wavenumber k_z . Also if $|\delta\mathbf{k}| \ll |\mathbf{k}|$ is not satisfied, it has been argued [17] that ν_{residual} is augmented by an amplitude dependent, but ν_{SideLoss} independent, form of Landau damping. However, as we discuss in Section IV B below, that addition to ν_{residual} is not consistent with our simulation results and we set $\nu_{\text{residual}} = 0$.

Eq. (24) may be used to find $\partial\omega/\partial\phi_{eq}$ in terms of $\partial v_\varphi/\partial\phi_{eq}$ which in turn may be obtained by applying $\partial/\partial\phi_{eq}$ to Eq. (22).

$$\{Re[\Xi'_0(v_\varphi)] - 1.76f_0''' \sqrt{\phi_{eq}}\} \frac{\partial v_\varphi}{\partial \phi_{eq}} = \frac{1.76f_0'''(v_\varphi)}{2\sqrt{\phi_{eq}}}. \quad (35)$$

In the kinetic regime, D may assume negative values as $|\delta\mathbf{k}|$ [8] and/or ϕ_{eq} [15] increase. Therefore, the qualitative shape of γ contours determined by Eqs. (22),

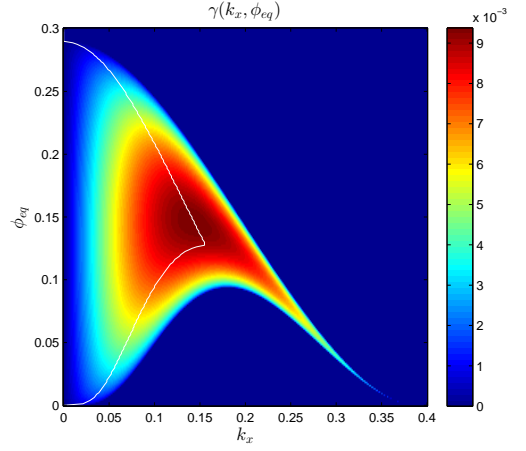


FIG. 5. (Color online) LW filamentation growth rate contours for $k_z = 0.35$. White line shows the maximum growth rate for given ϕ_{eq} .

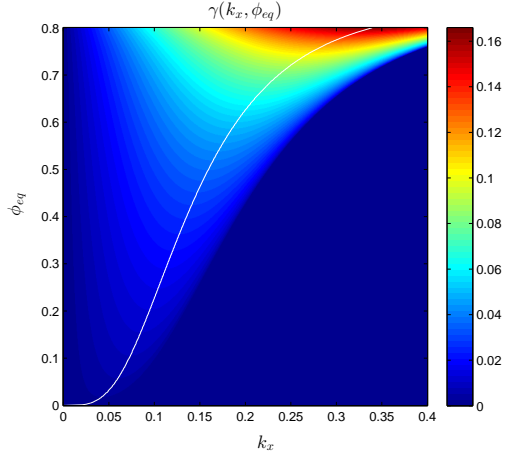


FIG. 6. (Color online) LW filamentation growth rate contours for $k_z = 0.35$ using linear approximation for D as in (32). White line shows the maximum growth rate for given ϕ_{eq} .

(29) and (30) may differ from fluid model modulational/filamentation [17], whose domain of applicability is limited, a priori, to $k_z \ll 1$. Contours of γ for $k_z = 0.35$ are shown in Figs. 5, with ν_{residual} set to 0. For more contours of γ and related figures see [15]. If we use linear approximation for D as in Eq. (32) and solve Eqs. (22), (29) for $k_z = 0.35$ and $\nu_{\text{residual}} = 0$ we get contours of γ as shown in Fig. 6. As k_z is increased, the range of amplitudes over which Eqs. (22), (29) and (30) predict growth is reduced, while using D_{lin} from Eq. (32) provides growth in a full range of amplitudes for any k_z . The latter case is more consistent with the simulations as we will see in Section IV.

Another simplification can be made if one assumes at the leading order that the nonlinear frequency shift $\Delta\omega \propto \sqrt{\phi_{eq}}$. Then $\phi_{eq} \frac{\partial \omega}{\partial \phi_{eq}} = \Delta\omega/2$ and maximizing γ over D

in Eq. (29) we obtain the maximum value

$$\gamma^{max} = |\Delta\omega|/4, \quad (36)$$

at

$$D = -\Delta\omega/4, \quad (37)$$

which is valid for $|\delta\mathbf{k}| \ll |\mathbf{k}|$ and $\nu_{residual} = 0$. Using the approximation (32), we obtain from Eq. (37) the position of the maximum

$$|\delta\mathbf{k}| = k_x^{max} = \left(\frac{-\Delta\omega k_z}{2v_g} \right)^{1/2}. \quad (38)$$

IV. NUMERICAL SIMULATIONS OF LW FILAMENTATION

Here we describe $2 + 2D$ fully nonlinear Vlasov simulations that we performed to study the filamentation instability of BGK modes described in the previous section.

A. Simulation settings and methods

We simulate $2 + 2D$ Vlasov-Poisson system (1)-(4) in phase space, (z, v_z, x, v_x) , using fully spectral (in all four dimensions) code and 2nd order in time split-step (operator splitting) method with periodic boundary conditions (BC) in all four dimensions. To ensure spectral convergence and imitate the weak effect of collisions, we added to Eq. (1) a small hyper-viscosity term as follows

$$\left\{ \frac{\partial}{\partial t} + v_z \frac{\partial}{\partial z} + v_x \frac{\partial}{\partial x} + E_z \frac{\partial}{\partial v_z} + E_x \frac{\partial}{\partial v_x} \right\} f = -D_{16v_z} \frac{\partial^{16}}{\partial v_z^{16}} \left(f - \frac{1}{L_z} \int_0^{L_z} f dz \right), \quad (39)$$

where D_{16v_z} is the 16th order hyper-viscosity coefficient. We use periodic BC in z direction with period $L_z = 2\pi/k_z$ and $k_z = 0.35$ in our simulations. Choosing $L_z = 2\pi/k_z$ allows us to focus on the study of filamentation instability effects (along x) while avoiding subharmonic (sideband) instability [42] in the longitudinal z -direction. Periodic BC in x with the period L_x together with x -independent initial condition (IC) are used to separate filamentation instability effects from any sideloss effects due to trapped electrons traveling in the transverse direction (this is in contrast to Ref. [43], where the transverse spatial profile in the initial condition made sideloss comparable with filamentation instability growth rate). We chose typically $200\pi \leq L_x \leq 800\pi$ depending on the BGK mode's amplitude to capture all growing transverse modes. Periodic BC in v_z and v_x were used without sacrificing any accuracy of the simulation compared to outgoing BC since the particle flow through the

boundary at $v_z = v_z^{max}$ is $\propto E_z \frac{\partial f}{\partial v_z}$ with $\frac{\partial f}{\partial v_z} \approx \frac{v_z}{\sqrt{2\pi}} e^{-\frac{v_z^2}{2}}$ which can be made as small as desired by picking large enough v_z^{max} . Typically we choose $v_z^{max} = 8$ for which $|E_z \frac{\partial f}{\partial v_z}| \approx 10^{-15}$. The same argument is applied in v_x direction with the only difference that in our simulations E_x is several orders less than E_z so v_x^{max} can be chosen smaller than v_z^{max} . Typically we choose $v_x^{max} = 6$ for which the flow through $v_x = v_x^{max}$ boundary is at the level of machine precision.

Split-step method of 2nd order was chosen over other methods since it is unconditionally stable (which allows large time steps), preserves number of particles at each time step exactly and has a very small error in the full energy of the system. That error is not accumulated over time (in contrast with Runge-Kutta methods where such accumulation occurs). We also decided to choose 2nd order method over higher order methods because our experiments with the size of time step and methods of various orders showed that the time integration error is dominated by the errors coming from other sources (space discretization and hyper-viscosity term).

The hyper-viscosity term in the right-hand side (r.h.s.) of Eq. (39) is used to prevent recurrence [44] and aliasing (which causes propagation of numerical error from high modes to low modes) effects. The hyper-viscosity operator in r.h.s. of Eq. (39) has to be a smooth function in the Fourier transformed v_z space. At the same time we found it beneficial to use high-order (here we choose 16th order) over low-order hyper-viscosity since it affects low modes of solution less while having effectively the same damping effect on high modes. That allows to use a smaller numerical grid for the same overall precision. The coefficient D_{16v_z} is chosen as small as possible to prevent aliasing depending on the resolution of simulation in v_z directions. Our safe estimate $D_{16v_z} \approx |\gamma_{Landau}(k_z)|(\frac{2\Delta v_z}{\pi})^{16}$ with $\gamma_{Landau}(k_z = 0.35) = -0.034318\dots$ found to be sufficient to avoid aliasing issues and completely remove the recurrence effect [44] in linear Landau damping simulations (while still recovering proper Landau damping with any desired accuracy for simulations with low-amplitude waves). Simulations with high amplitude waves (with $\Phi \sim 1$) might require higher value of hyper-viscosity coefficient D_{16v_z} , so one needs to keep track of spectrum of the solution in (z, v_z) space and adjust D_{16v_z} if needed. We typically used $D_{16v_z} = 10^{-25}$ for simulations with $N_z \times N_{v_z} = 64 \times 256$ grid points in (z, v_z) space and $D_{16v_z} = 10^{-30}$ for $N_z \times N_{v_z} = 128 \times 512$. Also hyper-viscosity does not affect conservation of number of particles in the system while having positive effect on conservation of energy in long-term simulations. While the term $-\frac{1}{L_z} \int_0^{L_z} f dz$ in r.h.s. side of (39) is not absolutely necessary, we found that the total energy of the system is conserved better if this term is used. This is because this term prevents filtering out of the 0th harmonic of f in z -space that holds most of the kinetic energy. We did not need any hyper-viscosity in v_x direction since the electrostatic field (and therefore both perturbations of

electron density and amount of energy in high modes) in transverse direction is many orders of magnitude weaker compared to the longitudinal direction (z, v_z) throughout most of the simulation until nonlinear self-focusing event at the end. Detailed simulation of that event is however outside of the scope of this paper.

All simulations are carried out in the lab frame rather than in moving frame, since in this case the tails of the distribution function in v_z direction are almost symmetric and have smaller values $\propto \exp(-(v_z^{max})^2/2)$ at the boundaries $\pm v_z^{max}$ compared to the tail value $\propto \exp(-(v_z^{max} - v_\phi)^2/2)$ in simulations done in the wave frame moving with velocity v_ϕ with the same v_z^{max} . For this reason simulations performed in the lab frame have smaller numerical error due to periodic BC in v_z .

B. 2+2D simulations and filamentation instability of 1D BGK modes

In these simulations we use IC of the form of Eq. (7) that has the constructed BGK mode from Section III A in the (z, v_z) directions, uniform in the x -direction and a Maxwellian distribution $f_0(v_x)$ in the v_x direction,

$$f(z, v_z, x, v_x, t = 0) = f_{BGK}(z, v_z)f_0(v_x). \quad (40)$$

We run simulations for a long enough time to observe the growth of oblique harmonics of electric field with wave vectors $(k_z = 0.35, k_x)$ (see Fig. 7 for a quarter of $E_z(z, x)$ spectrum, other quarters of the spectrum are similar to it) for several orders in magnitude (see Fig. 8), where k_z is the wavenumber corresponding to the BGK mode and k_x varies between $-k_x^{max}$ and $k_x^{max} = \pi/\Delta x$, $\Delta x = L_x/N_x$, where N_x is the number of grid points in x . The initial values in these harmonics are near the machine precision from the round-off errors. During the simulation they grow from values $\sim 10^{-16}$ to $\sim 10^{-1}$. The exponential growth rates γ_{k_x} for these harmonics are extracted (see Fig. 9) from the least-square fit when the amplitudes grow from $\sim 10^{-13}$ to $\sim 10^{-8} - 10^{-6}$ (during these times a clear exponential growth $\propto e^{\gamma_{k_x} t}$ is observed). Later in the simulation, nonlinear self-focusing effects come into play and LW filamentation occurs (see Figs. 10 and 11) transferring a significant part of electric field energy, $P(t) = \iint \frac{|E_z|^2 + |E_x|^2}{2} dz dx$, into kinetic energy, $K(t) = \iiint \frac{(v_z^2 + v_x^2)}{2} f dz dx dv_z dv_x$ (see Fig. 12). Notice also that the relative error in full energy of the system, $\text{Energy}(t) = P(t) + K(t)$, is small. Figs. 7-12 are obtained from the simulation with $\phi_{eq} = 0.2$. Other simulation parameters were $D_{16v_z} = 10^{-25}$, $64 \times 256 \times 64 \times 32$ grid points for (z, v_z, x, v_x) with $L_z = 2\pi/k_z$, $L_x = 400\pi$, $v_z^{max} = 8$, $v_x^{max} = 6$, the time step $\Delta t = 0.1$ and the final simulation time $T_{final} = 5000$. Simulations with a larger L_x and correspondingly larger extent of spectrum in k_x were done too but no other regions of growing modes in spectrum (such as in Figs. 7 and 9) were observed except for the one starting near $k_x = 0$.

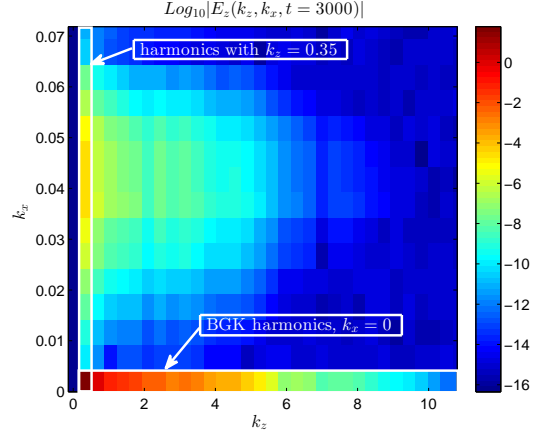


FIG. 7. (Color online) The density plot of the spectrum of $E_z(z, x)$ at $t = 3000$.

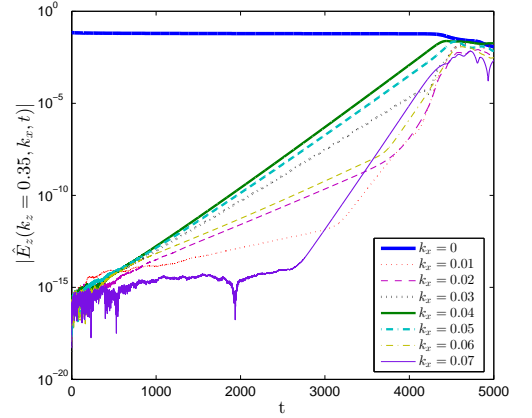


FIG. 8. (Color online) The growth of harmonics $|\hat{E}_z(k_z = 0.35, k_x, t)|$ in time.

These simulations were done for a variety of BGK modes with $k_z = 0.35$, amplitudes $0.025 \leq \phi_{eq} \leq 0.77$ and values of v_ϕ according to the BGK dispersion relation (22). The parameters of these simulation were $D_{16v_z} = 10^{-25}$, $64 \times 256 \times 32 \times 32$ grid points for (z, v_z, x, v_x) , $\Delta t = 0.1$ and $2000 \leq T_{final} \leq 30000$ (depending on BGK amplitude). Another set of simulations was performed for $D_{16v_z} = 10^{-30}$ and $128 \times 512 \times 32 \times 32$ grid points with the rest of parameters being the same.

We extract the nonlinear frequency shift $\Delta\omega^{NUM}$ from simulations by finding the wave frequency as the rate of change of the phase of the Fourier harmonic of Φ with $k_z = 0.35, k_x = 0$ and subtracting the frequency that corresponds to our undamped BGK mode in the limit of zero amplitude, $\omega_0 = \omega(k_z = 0.35, \phi_{eq} = 0) = 1.2116687\dots$, which can be found as a real root of $\text{Re}[\varepsilon_0(k_z, \omega)] = 0$ or Eq. (22) with $\phi_{eq} = 0$. Note that the frequency of the damped linear LW (real part of a complex root of $\varepsilon_0(k_z, \omega) = 0$ [3, 4]) is $\omega_{LW}(k_z = 0.35) = 1.22095\dots$, for the discussion of Vlasov vs. Landau analysis see Ref. [34]. The difference is $\approx 1\%$ for $k_z = 0.35$ and it becomes

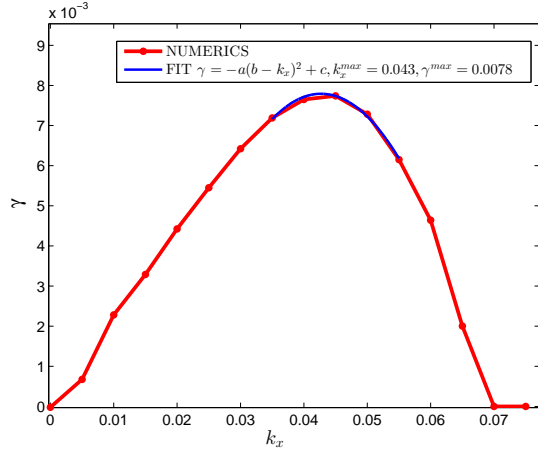


FIG. 9. (Color online) The growth rates γ_{k_x} of oblique harmonics extracted from the least-square fit to the data of Fig. 8. A fit to the quadratic law near the maximum is also shown.

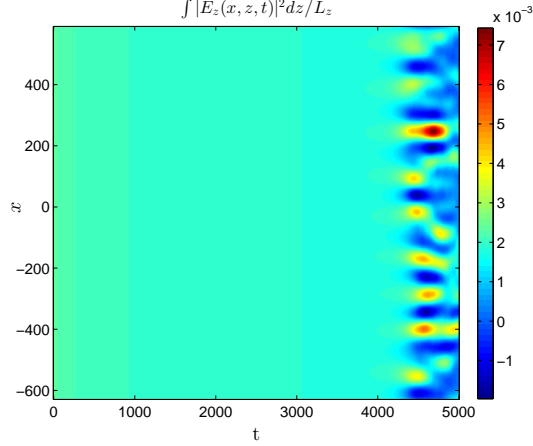


FIG. 10. (Color online) The density plot vs. x and t for $\langle |E_z|^2 \rangle_z \equiv L_z^{-1} \int_0^{L_z} |E_z|^2 dz$ ($|E_z|^2$ averaged over z) shows a development of LW filamentation with time from the initial BGK mode.

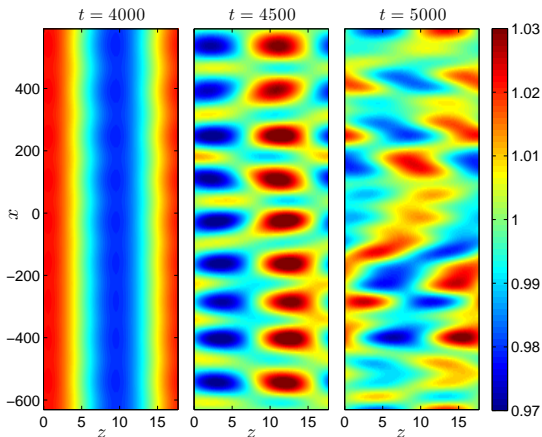


FIG. 11. (Color online) Modulation of particle density $\rho(z, x)$ before ($t = 4000$), during ($t = 4500$) and after ($t = 5000$) Langmuir wave filamentation.

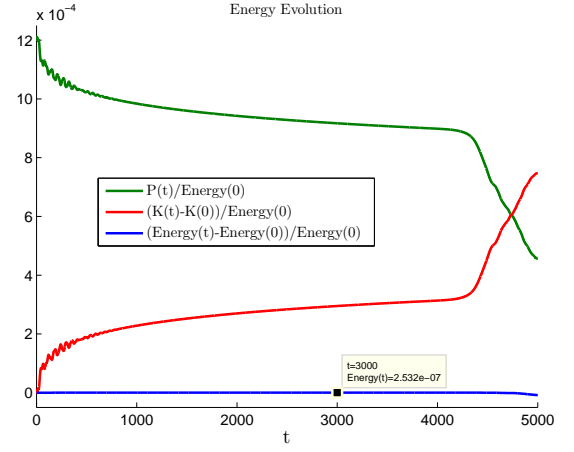


FIG. 12. (Color online) Evolution of electrostatic, $P(t)$, kinetic, $K(t)$, and total energy, $\text{Energy}(t)$, in the simulation with BGK amplitude $\phi_{eq}=0.2$.

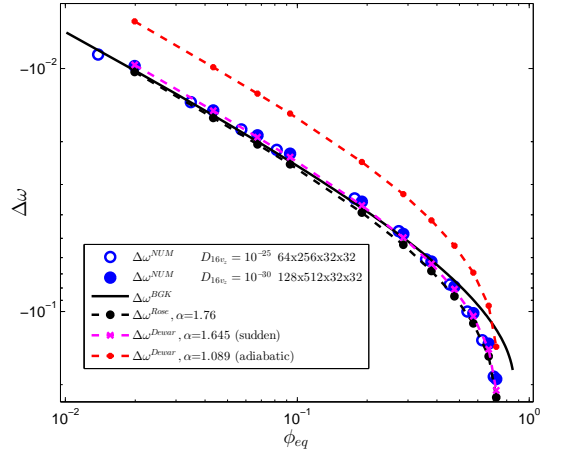


FIG. 13. (Color online) Nonlinear frequency shift as a function of BGK amplitude ϕ_{eq} .

larger for larger k_z . Fig. 13 shows $\Delta\omega^{NUM}$ (large circles (blue color online)) obtained from simulations in comparison with theoretical one $\Delta\omega^{BGK}$ (solid black line) computed using Eq. (25), approximations $\Delta\omega_{NL}^{Rose}$ (dashed black line with circle markers) and $\Delta\omega^{Dewar}$ (dashed grey lines with small “o” (red online) and “x” (pink online) markers) given by Eqs. (26) and (27), respectively, for which we used $v_\varphi = \omega^{NUM}/k_z$. We conclude from Fig. 13 that both $\Delta\omega_{NL}^{Rose}$ and $\Delta\omega^{Dewar}$ with $\alpha = 1.645$ (sudden) work really well for the whole range of amplitudes whereas $\Delta\omega^{BGK}$ works well for amplitudes of BGK $\phi_{eq} \lesssim 0.5$ since v_φ for $\phi_{eq} > 0.5$ deviates from the solution of approximate dispersion relation Eq. (22) as can be seen in Fig. 4.

Growth rates of filamentation instability as a function of k_x from the series of simulations with $D_{16v_z} = 10^{-30}$ and various amplitudes ϕ_{eq} are given in Figs. 14 and 15. The maximum growth rate γ^{max} (the maximum vs. k_x for each fixed ϕ_{eq}) as a function of ϕ_{eq} is shown

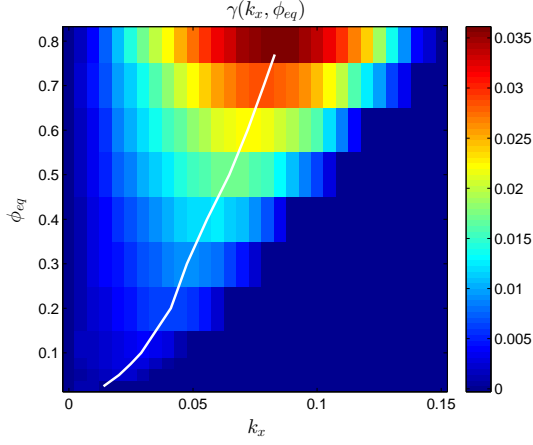


FIG. 14. (Color online) Numerical growth rates γ density plot as a function of k_x and BGK amplitude ϕ_{eq} . The white line shows the position of the maximum γ_{k_x} for each ϕ_{eq} .

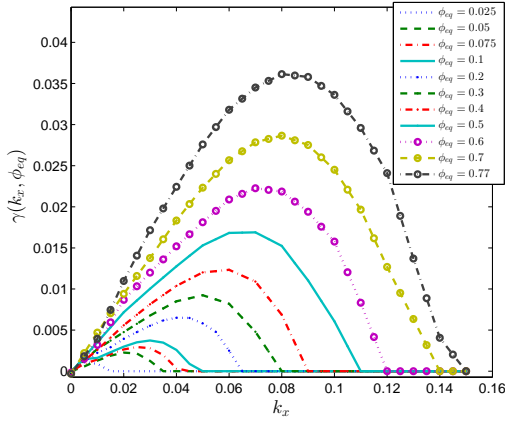


FIG. 15. (Color online) The growth rates γ_{k_x} as a function of k_x for BGK modes with various amplitudes ϕ_{eq} correspond to multiple cross-sections of Fig. 14.

in Fig. 16 (for $D_{16v_z} = 10^{-30}$ and $D_{16v_z} = 10^{-25}$, filled and non-filled circles, respectively) together with the theoretical predictions given by Eqs. (22), (24), (29) and (31) (dashed-dotted line of light grey (orange online) color) and given by Eqs. (29) and (32) (dashed-dotted line of dark grey (brown online) color). Other lines in Fig. 16 use the leading order approximation in ϕ_{eq} given by Eq. (36) with four estimates for $\Delta\omega$: from simulations $\Delta\omega = \Delta\omega^{NUM}$; from Eq. (26) $\Delta\omega = \Delta\omega_{NL}^{Rose}$ and $\Delta\omega = \Delta\omega_{NL}^{Dewar}$ for two cases of Eq. (27).

We conclude from Fig. 16 that while theoretical prediction based on Eqs. (22), (24), (29) and (31) claims no growth for the amplitudes $\phi_{eq} \gtrsim 0.3$, we still observe growth for even higher amplitudes. Eqs. (29) and (32) predict growth for any amplitudes but differ from the numerical results by $\sim 70\%$ while approximations $\gamma^{max} \approx |\Delta\omega_{Rose}|/4$, $\gamma^{max} \approx |\Delta\omega^{NUM}|/4$ and $\gamma^{max} \approx |\Delta\omega^{Dewar}|/4$ with $\alpha = 1.645$ (sudden) work better, especially for amplitudes $\phi_{eq} > 0.1$, staying almost identi-

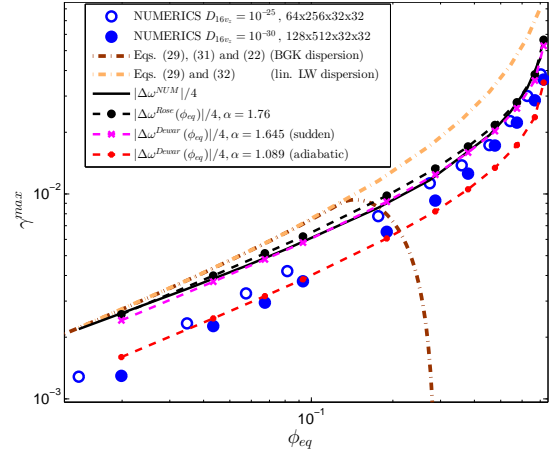


FIG. 16. (Color online) The maximum growth rate as a function of BGK amplitude ϕ_{eq} .

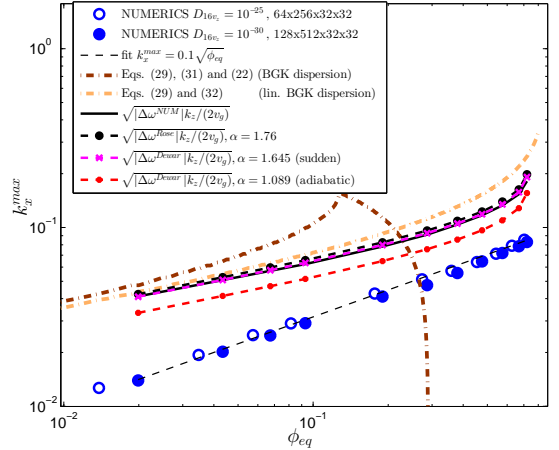


FIG. 17. (Color online) The wavenumber k_x^{max} at which the growth rate reaches the maximum as a function of BGK amplitude ϕ_{eq} .

cal to each other. While including $\gamma^{max} \approx |\Delta\omega^{Dewar}|/4$ with $\alpha = 1.089$ (adiabatic) curve into Fig. 16 for comparison, we believe that it's most appropriate to compare the numerical results to $\gamma^{max} \approx |\Delta\omega^{Dewar}|/4$ with $\alpha = 1.645$ (sudden) as Fig. 13 clearly shows that an actual frequency shift $\Delta\omega^{NUM}$ is much closer to $\Delta\omega^{Dewar}$ with “sudden” distribution rather than “adiabatic” one. In all these comparisons with theory we assumed in Eq. (29) that $\nu_{residual} = 0$ consistent with the expected absence of sideloss in the periodic BC in x as discussed in the beginning of Section IV. Landau damping, for modes that propagate at some finite angle, is neglected. The authors are not aware of any satisfactory model for such in the literature. That which is available [17] is ad hoc and fails to properly describe the nonlinear frequency shift. It predicts approximately twice larger nonlinear frequency shift for a wave of given amplitude than the nonlinear frequency shift that Dewar’s sudden model or the actual frequency shift of our BGK modes.

The wavenumber $k_x = k_x^{max}$ at which the growth rate has the maximum is shown in Fig. 17 as a function of ϕ_{eq} together with the theoretical predictions. Dashed-dotted line of sand color represents prediction by Eqs. (22), (24), (29) and (31), dashed-dotted line of brown color represents prediction by Eqs. (29) and (32), other lines in Fig. 17 use the leading order approximation in ϕ_{eq} given by Eq. (38) with the BGK mode group velocity v_g defined in Eq. (32). They include different estimates of $\Delta\omega$, from Rose's model (26), Dewar's model (27) and measured $\Delta\omega^{NUM}$. The equation (38) predicts $k_x^{max} \propto \sqrt{\Delta\omega}$, which in case of $\Delta\omega \propto \sqrt{\phi_{eq}}$ as in Eqs. (26) and (27) becomes $k_x^{max} \propto (\phi_{eq})^{1/4}$ and fails to agree with numerical results for k_x^{max} somewhat well as seen in Fig. 17. It is also seen in Fig. 17 that the empirical dependence $k_x^{max} \sim 0.1\sqrt{\phi_{eq}}$ fits the numerical results pretty well but remains to be explained theoretically.

We also investigated the convergence of growth rates with $D_{16v_z} \rightarrow 0$ while $\Delta z, \Delta v_z \rightarrow 0$ and, correspondingly, $N_z, N_{v_z} \rightarrow \infty$ while keeping $N_x = 32, N_{v_x} = 32$ (the discretization in x space does not affect the error in growth rates and 32 points in v_x space together with $v_x^{max} = 6$ are enough to resolve the Maxwellian distribution in v_x direction with error $< 10^{-8}$). We found that the relative errors in our numerical results for growth rates with $D_{16v_z} = 10^{-30}$ and $128 \times 512 \times 32 \times 32$ grid points for (z, v_z, x, v_x) are within 10 – 15% range. Reducing Δt affected the growth rates results even less so we concluded that $\Delta t = 0.1$ was sufficient.

C. Comparison of filamentation instability growth rates with PIC code simulations

We now compare γ_{k_x} that we obtained in Section IV B from our simulations for the mode with $(k_z = 0.35, k_x = 0.05)$ to the growth rates of the same mode obtained using PIC simulations in Fig. 9(j) of Ref. [16] for three different amplitudes of BGK modes: $\phi_{eq} = 0.2, 0.3, 0.5$. These BGK modes in both cases were constructed using $k_z = 0.35$ and have $v_\phi = 3.35818, 3.32288, 3.23266$, respectively. Our growth rates for these three amplitudes are 0.0073, 0.0113 and 0.0158. The corresponding growth rates from Ref. [16] are 0.0075, 0.012, and 0.0147, i.e. only $\sim 10\%$ difference with our results. The total number of particles used in Ref. [16] was $\approx 2 \times 10^8$ with 32×1280 cells and 5000 particles per cell. Number of grid points in our simulations was $64 \times 256 \times 32 \times 32$ for (z, v_z, x, v_x) (total $\approx 1.6 \times 10^7$) with $L_z = 2\pi/k_z, L_x = 200\pi, v_z^{max} = 8, v_x^{max} = 6$, and $D_{16v_z} = 10^{-25}, \Delta t = 0.1, T_{final} = 5000$.

V. CONCLUSION AND DISCUSSION

We studied the linear Langmuir wave (LW) filamentation instability of a particular family of BGK modes that bifurcates from a linear periodic Langmuir wave for $k\lambda_D = 0.35$. These BGK modes approximate the non-linear electron plasma wave resulting from adiabatically slow pumping by SRS. The construction process of these BGK modes is described in detail. Performing direct 2+2D Vlasov-Poisson simulations of collisionless plasma we found that the maximal growth rates from simulations are 30 – 70% smaller compared to the theoretical prediction but exhibit the proper scaling for small amplitudes of BGK wave $\gamma^{max} \propto \sqrt{\phi_{eq}}$ while $k_x^{max} \propto \sqrt{\phi_{eq}}$. These results await an improved theory since current theory predicts $k_x^{max} \propto (\phi_{eq})^{1/4}$.

This behavior contrasts strongly with LW propagation [4] in the “fluid” regime, $k\lambda_D \lesssim 0.2$, in which both two-dimensional (2D) and three-dimensional (3D) collapse [13, 45, 46] may occur if we take into account ion dynamics. Consider a LW wavepacket with electric field amplitude E . Its ponderomotive force causes a localized plasma density hole, $\delta n \propto -|E|^2$, which localizes and enhances $|E|$, creating a deeper and narrower hole in the plasma density, and so on, leading to yet larger values of $|E|$ until Landau damping terminates this “collapse” process.

As shown in Ref. [8], the transition from the fluid to the regime where the trapped electron effects cannot be ignored occurs at $k\lambda_D \sim 0.2$. Thus at $k\lambda_D \gtrsim 0.2$. LW frequency reduction due to electron trapping may dominate [8] the ponderomotive [4] frequency shift [11, 14] with $\Delta\omega \propto |E|^2$. Contrary to the result of Ref. [14] where fluid nonlinearity frequency shift $\Delta\omega_{fluid}$ is shown to be positive via use of water bag distribution of electrons, the result of Ref. [11] indicates that $\Delta\omega_{fluid}$ can have either sign depending on k , for example in case of Maxwellian distribution. Refs. [14] and [11] suggest that kinetic effects might dominate fluid effects even for large amplitudes of LW if $k\lambda_D > 0.3$. Though the trapped electron frequency shift, perturbatively, varies as $|E|^{1/2}$ [6, 9, 10], and therefore cannot lead to LW collapse [13, 45, 46], 3D PIC simulation results [18] have been interpreted as showing that the trapped electron LW filamentation instability can saturate [19] stimulated Raman back-scatter (SRS) [21] by reducing the LWs coherence.

Since experimental data in the kinetic LW regime is at best qualitative and indirect, such as furnished by observations of SRS light, first principle Vlasov simulations and theory appear to be the chief tools for analyzing LW properties in the kinetic regime. Because LW filamentation is a multi-dimensional effect, with qualitatively different [19] 2D versus 3D nonlinear behavior, analysis via Vlasov numerical solutions will remain an outstanding challenge.

ACKNOWLEDGMENTS

This work was supported by the National Science Foundation under Grants No. PHY 1004118, No. PHY 1004110 and DMS-1412140. Simulations were per-

formed at the Center for Advanced Research Computing (CARC) at the University of New Mexico and the Texas Advanced Computing Center (TACC) which was supported by National Science Foundation Grant ACI-1053575.

-
- [1] H. A. Rose and D. A. Russell, *Physics of Plasmas* **8**, 4784 (2001).
 - [2] I. B. Bernstein, J. M. Greene, and M. D. Kruskal, *Phys. Rev.* **108**, 546 (1957).
 - [3] E. M. Lifshitz and L. Pitaevskii, *Physical Kinetics: Volume 10* (Butterworth-Heinemann, Oxford, 1981).
 - [4] D. R. Nicholson, *Introduction to Plasma Theory*, Vol. XII (John Wiley & Sons, New York, 1983).
 - [5] T. P. Coffey, *The Physics of Fluids* **14**, 1402 (1971).
 - [6] R. L. Dewar, *Physics of Fluids* **15**, 712 (1972).
 - [7] R. L. Dewar and J. Lindl, *The Physics of Fluids* **15**, 820 (1972).
 - [8] H. A. Rose, *Physics of Plasmas* **12**, 012318 (2005).
 - [9] W. M. Manheimer and R. W. Flynn, *Physics of Fluids* **14**, 2393 (1971).
 - [10] G. J. Morales and T. M. O'Neil, *Phys. Rev. Lett.* **28**, 417 (1972).
 - [11] C. Liu and I. Y. Dodin, *Physics of Plasmas* **22**, 082117 (2015).
 - [12] J. L. Kline, D. S. Montgomery, B. Bezzerides, J. A. Cobble, D. F. DuBois, R. P. Johnson, H. A. Rose, L. Yin, and H. X. Vu, *Phys. Rev. Lett.* **94**, 175003 (2005).
 - [13] J. L. Kline, D. S. Montgomery, L. Yin, D. F. DuBois, B. J. Albright, B. Bezzerides, J. A. Cobble, E. S. Dodd, D. F. DuBois, J. C. Fernandez, R. P. Johnson, J. M. Kindel, H. A. Rose, H. X. Vu, and W. Daughton, *Physics of Plasmas* **13**, 055906 (2006).
 - [14] B. Winjum, J. Fahlen, and W. Mori, *Physics of Plasmas* **14**, 102104 (2007).
 - [15] H. A. Rose and L. Yin, *Physics of Plasmas* **15**, 042311 (2008).
 - [16] L. Yin, B. J. Albright, K. J. Bowers, W. Daughton, and H. A. Rose, *Physics of Plasmas* **15**, 013109 (2008).
 - [17] R. L. Berger, S. Brunner, J. W. Banks, B. I. Cohen, and B. J. Winjum, *Physics of Plasmas* **22**, 055703 (2015).
 - [18] K. J. Bowers, B. J. Albright, L. Yin, B. Bergen, and T. J. T. Kwan, *Physics of Plasmas* **15**, 055703 (2008).
 - [19] L. Yin, B. J. Albright, H. A. Rose, K. J. Bowers, B. Bergen, D. S. Montgomery, J. L. Kline, and J. C. Fernandez, *Physics of Plasmas* **16**, 113101 (2009).
 - [20] L. Yin, B. J. Albright, H. A. Rose, D. S. Montgomery, J. L. Kline, R. K. Kirkwood, J. Milovich, S. M. Finnegan, B. Bergen, and K. J. Bowers, *Physics of Plasmas* **21**, 092707 (2014).
 - [21] M. V. Goldman and D. F. Du Bois, *Physics of Fluids* **8**, 1404 (1965).
 - [22] D. A. Russell, D. F. DuBois, and H. A. Rose, *Physics of Plasmas* **6**, 1294 (1999).
 - [23] D. S. Montgomery, J. A. Cobble, J. C. Fernandez, R. J. Focia, R. P. Johnson, N. Renard-LeGalloudec, H. A. Rose, and D. A. Russell, *Physics of Plasmas* **9**, 2311 (2002).
 - [24] C. E. Max, J. Arons, and A. B. Langdon, *Phys. Rev. Lett.* **33**, 209 (1974).
 - [25] S. Depierreux, V. Yahia, C. Goyon, G. Loisel, P. E. Masson-Laborde, N. Borisenko, A. Orekhov, O. Rosmej, T. Rienecker, and C. Labaune, *Nature Communications* **5**, 4158 (2014).
 - [26] A. J. Schmitt and B. B. Afeyan, *Physics of Plasmas* **5**, 503 (1998).
 - [27] P. M. Lushnikov and H. A. Rose, *Plasma Physics and Controlled Fusion* **48**, 1501 (2006).
 - [28] P. M. Lushnikov and H. A. Rose, *Phys. Rev. Lett.* **92**, 255003 (2004).
 - [29] H. A. Rose and W. Daughton, *Physics of Plasmas* **18**, 122109 (2011).
 - [30] Y. Kato, K. Mima, N. Miyanaga, S. Arinaga, Y. Kitagawa, M. Nakatsuka, and C. Yamanaka, *Phys. Rev. Lett.* **53**, 1057 (1984).
 - [31] J. D. Lindl, P. Amendt, R. L. Berger, S. H. G. S. G. Glendinning, S. W. Haan, R. L. K. O. L. Landen, and L. J. Suter, *Phys. Plasmas* **11**, 339 (2004).
 - [32] N. B. Meezan, L. J. Atherton, D. A. Callahan, E. L. Dewald, S. Dixit, E. G. Dzenitis, M. J. Edwards, C. A. Haynam, D. E. Hinkel, O. S. Jones, O. Landen, R. A. London, P. A. Michel, J. D. Moody, J. L. Milovich, M. B. Schneider, C. A. Thomas, R. P. J. Town, A. L. Warrick, S. V. Weber, K. Widmann, S. H. Glenzer, L. J. Suter, B. J. MacGowan, J. L. Kline, G. A. Kyrala, and A. Nikroo, *Phys. Plasmas* **17**, 056304 (2010).
 - [33] J. P. Holloway and J. J. Dornig, *Phys. Rev. A* **44**, 3856 (1991).
 - [34] M. Buchanan and J. Dornig, *Phys. Rev. E* **52**, 3015 (1995).
 - [35] T. O'Neil, *Physics of Fluids* **8**, 2255 (1965).
 - [36] A. A. Vlasov, *Soviet Physics Uspekhi* **10**, 721 (1968).
 - [37] L. D. Landau, *J. Phys. (USSR)* **10**, 25 (1946), [*Zh. Eksp. Teor. Fiz.* 16, 574 (1946)].
 - [38] B. D. Fried, M. Gell-Mann, J. D. Jackson, and H. W. Wyld, *Journal of Nuclear Energy. Part C, Plasma Physics, Accelerators, Thermonuclear Research* **1**, 190 (1960).
 - [39] D. S. Montgomery, R. J. Focia, H. A. Rose, D. A. Russell, J. A. Cobble, J. C. Fernández, and R. P. Johnson, *Phys. Rev. Lett.* **87**, 155001 (2001).
 - [40] C. Lancellotti and J. J. Dornig, *Phys. Rev. Lett.* **81**, 5137 (1998).
 - [41] R. L. Berger, S. Brunner, T. Chapman, L. Divol, C. H. Still, and E. J. Valeo, *Physics of Plasmas* **20**, 032107 (2013).
 - [42] W. L. Kruer, J. M. Dawson, and R. N. Sudan, *Phys. Rev. Lett.* **23**, 838 (1969).
 - [43] P. M. Lushnikov, H. A. Rose, D. A. Silantyev, and N. Vladimirova, *Phys. of Plasmas* **21**, 072103 (2014).
 - [44] C. Cheng and G. Knorr, *J. of Comp. Phys.* **22**, 330 (1976).
 - [45] V. E. Zakharov, *Sov. Phys. JETP* **35**, 908 (1972).
 - [46] V. E. Zakharov, *Zh. Eksp. Teor. Fiz.* **62**, 1745 (1972).